Experiment and Theory on the Nonlinear Vibration of a Shallow Arch Under Harmonic Excitation at the End

Jen-San Chen
Professor
e-mail: jschen@ccms.ntu.edu.tw

Cheng-Han Yang

Department of Mechanical Engineering,
National Taiwan University,
Taipei, Taiwan 10617

*In this paper we study, both theoretically and experimentally, the nonlinear vibration of a shallow arch with one end attached to an electro-mechanical shaker. In the experiment we generate harmonic magnetic force on the central core of the shaker by controlling the electric current flowing into the shaker. The end motion of the arch is in general not harmonic, especially when the amplitude of lateral vibration is large. In the case when the excitation frequency is close to the n*th *natural frequency of the arch, we found that geometrical imperfection is the key for the n*th *mode to be excited. Analytical formula relating the amplitude of the steady state response and the geometrical imperfection can be derived via a multiple scale analysis. In the case when the excitation frequency is close to two times of the n*th *natural frequency two stable steady state responses can exist simultaneously. As a consequence jump phenomenon is observed when the excitation frequency sweeps upward. The effect of geometrical imperfection on the steady state response is minimal in this case. The multiple scale analysis not only predicts the amplitudes and phases of both the stable and unstable solutions, but also predicts analytically the frequency at which jump phenomenon occurs.* [DOI: 10.1115/1.2165231]

1 Introduction

Historically, the interest in shallow arch research is primarily on the snap-through buckling when the arch is under some kind of lateral loading. The first theoretical prediction on the static critical load was conducted by Timoshenko in 1935 [1], in which a pinned sinusoidal arch was subjected to a uniformly distributed load. Timoshenko's pioneering work was followed and extended by many other researchers on various kinds of topics, including the snap-through phenomenon under dynamic load. The first theoretical prediction of dynamic buckling load was conducted by Hoff and Bruce in 1954 [2], in which they studied the stability of a sinusoidal arch under unit step loading and ideal impulsive loading. A good introduction and more references on the static and dynamic snap-through buckling can be found in the two books by Simitses [3,4]. A more up-to-date reference list on these subjects can be found in a recently published paper by Chen and Liao [5].

Besides the quasi-static, impulsive, and step loadings discussed above, the dynamic response of a shallow arch under periodic excitation has also been studied by some researchers. Previous research in this regard may be roughly divided into two groups. The first group considers the case when the vibration amplitude is so large that dynamic snap-through occurs. The critical load amplitude and frequency of an arch under harmonic excitation is harder to predict compared to the problem of step or impulsive loading. Huang [6] used a cycle-averaging approach to predict the critical load when the excitation frequency is high. Plaut and Hsieh [7] used a one-term approximation to numerically study the critical load when the arch is subject to a two-frequency excitation. Blair et al. [8] simplified the arch with a two-rigid-link model and used harmonic balance method to study its dynamic response when it is under harmonic excitation.

The second group focuses on smaller excitation and vibration amplitude with emphasis on the nonlinear response such as superharmonic, subharmonic, and internal resonances. Thompson [9] studied the chaotic vibration of a circular high arch loaded by a harmonic force at its crown, a problem initiated by Boloton in his book [10]. Tien and Sri Namachchivaya [11,12] and Bi and Dai [13] used a two-term approximation to study the internal resonance of a shallow arch under lateral loading with both averaging method and direct integration method. With the same two-term approximation, Malhotra and Sri Namachchivaya [14,15] also investigated the possibility of chaotic response when the shallow arch is under 1:1 and 1:2 resonances.

From the above literature review we notice that while some theoretical investigations on the dynamic response of a periodically excited shallow arch exist, experimental investigation is relatively rare. Generally speaking, theoretical investigations tend to oversimplify the reality. For instance, it is not an easy matter to realize a pulsating load with constant amplitude in the laboratory because the structure will change the characteristics of the loading mechanism, especially when the vibration amplitude becomes large. For the internal resonance phenomenon discussed in Refs. [11–15], it can occur only when special relations among the natural frequencies of the arch happen to exist. In the real world, this situation occurs only accidentally.

One of the values of experimental work is that it can sometimes inspire new research ideas and help us establish more realistic model for analysis. In this paper we set out to design an experimental setup aiming to observe the nonlinear vibration of a shallow arch with an electro-mechanical shaker attached to one end. Special attention is focused on the case when the excitation frequency is close to the *n*th natural frequency (coupling resonance) and two times of the *n*th natural frequency (parametric resonance). Although the vibration phenomenon is nonlinear in nature the vibration amplitude of the arch is limited to be small enough so that no snap-through buckling will occur. The experimental observation is then compared to the numerical simulation based on the theoretical model. In order to capture the physical essence of the nonlinear vibration observed in the experiment and numerical simulation, we also develop an analytical technique based on the

Contributed by the Applied Mechanics Division of ASME for publication in the JOURNAL OF APPLIED MECHANICS. Manuscript received May 21, 2005; final manuscript received November 7, 2005. Review conducted by N. Sri Namachchivaya.

 Copyright © 2007 by ASME

Downloaded 16 Oct 2008 to 140.112.113.225. Redistribution subject to ASME license or copyright; see http://www.asme.org/terms/Terms_Use.cfm

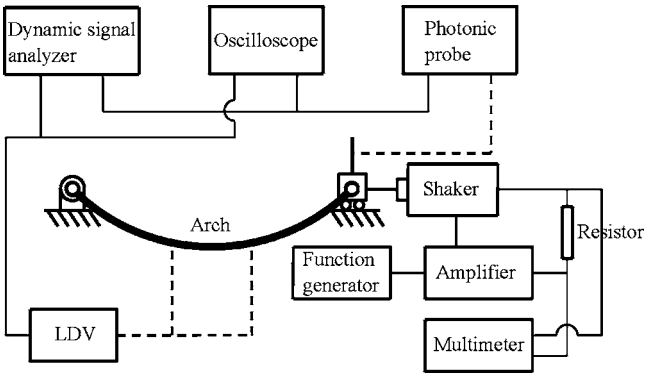

Fig. 1 Schematic diagram of the experimental setup

multiple scale method to formulate the closed-form solution of the steady state response of the arch. The theoretical and experimental results agree reasonably well.

2 Experimental Setup

Figure 1 is a schematic diagram of the experimental setup. The arch is made of copper strip with Young's modulus 101 GPa and mass density 8840 kg/m^3. The length L of the arch is 44 cm and the cross section is 25 mm$\times$1.2 mm. Both ends of the curved beam are attached to roller bearings to simulate pinned condition. One end of the arch is attached to an electro-magnetic shaker via a stinger. The magnetic force on the central core of the shaker is controlled by the current flowing into the shaker. A power amplifier connected to the shaker is responsible for pumping electric current proportional to the harmonic voltage signal from a function generator. The current can be monitored by measuring the voltage across a high-power low-ohm resistor. With this arrangement, the magnetic force on the central core of the shaker can be estimated accurately. Linear bearing is installed to reduce the friction when the end attachment slides on the guiding rods. The total mass of the bearing installation at the end is measured as m_e =0.8 kg. The axial motion of the sliding end is monitored by a photonic probe (MTI 2000). The lateral speeds at various locations of the arch are measured by a two-channel LDV system. The speed signals from the LDV system can be integrated to obtain the displacement history.

Although the arch is designed to match a half-sinusoidal curve as closely as possible, some minor deviation can still be detected. This deviation is the geometrical imperfection. It will be shown that these minor imperfections are of paramount importance when the excitation frequency of the shaker is close to one of the natural frequencies of the arch. We assume that the initial shape of the arch y_0, measured from the base line passing through the two ends, can be expanded in a Fourier series

$$y_0 = \sum_{n=1}^{\infty} h_n \sin \frac{n\pi x}{L} \tag{1}$$

To determine the coefficients of various Fourier components in Eq. (1), we measure the deviation of the arch to the designed half-sinusoidal curve at 40 equidistant locations. By employing a least-squares method we can estimate the first eight harmonic components h_1–h_8, as listed in Table 1. The second row of Table 1 lists the physical height h_n. The third row lists the dimensionless height h_n^*, whose definition can be found in Eq. (5) later. It is noted that the initial shape of the specimen is indeed very close to the half-sinusoidal shape with h_1 being the dominant coefficient. Most of the coefficients corresponding to the imperfection (h_n with $n \geq 2$) are on the order of less than 1% of h_1, except h_3 which amounts to 6.4% of h_1.

Table 1 Coefficients of Fourier expansion of the initial shape. The second row lists the physical height h_n. The third row lists the dimensionless height h_n^*.

n	1	2	3	4	5	6	7	8
h_n (mm)	16.10	−0.19	−1.03	0.14	0.06	−0.01	−0.005	0.003
h_n^*	46.5	−0.55	−2.98	0.41	0.18	−0.04	−0.014	0.01

As a first approximation, the central core and suspension of the shaker is modeled as a one degree-of-freedom mass-spring oscillator. The natural frequency of this central core-suspension system is measured at 114.88 Hz. The spring constant of the suspension is estimated as k=22253 N/m by measuring the displacements (with power off) of the central core when different forces (weights) are applied. The effective mass of the oscillator is then calculated as m_s=0.043 kg. We are not interested in the damping of the shaker at this stage because we are more interested in the damping of the whole system when the shaker is attached to the movable end of the arch. When the central core is connected to the movable end of the arch in series, the total mass m=0.843 kg will be the combination of m_e and m_s. The theoretical model of our experimental setup is shown in Fig. 2. It is noted that while we can control the force on the end mass m by controlling the electric current flowing into the shaker, we cannot control the motion e of the end mass. Therefore, the experimental setup is under load control.

3 Equations of Motion

Consider the theoretical model shown in Fig. 2. The two pinned ends of the elastic shallow arch are originally separated by a distance L. The arch is free of lateral loading. At one end, the arch is connected to a sliding mass m, which is restrained by a spring k. The mass is subjected to a harmonic excitation force $2f \cos \gamma t$, where $2f$ and γ are the amplitude and the frequency of the force. The initial and deformed shapes of the arch are y_0 and y, both measured from the same baseline. The equation of motion of the arch can be written as

$$\rho A y_{,tt} = -EI(y - y_0)_{,xxxx} + p y_{,xx} \tag{2}$$

The parameters E, ρ, A, and I are Young's modulus, mass density, area, and area moment of inertia of the cross section of the arch. p is the axial force in the deformed arch. The force balance of the attached end mass gives an additional equation

$$m\ddot{e} = -p - ke + 2f \cos \gamma t \tag{3}$$

The relation between the end motion e and the shape change of the arch can be established from the elastic extensibility of the arch

$$p = \frac{EA}{L}\left\{ e + \frac{1}{2}\int_0^L [(y_{,x})^2 - (y_{0,x})^2]dx \right\} \tag{4}$$

After replacing the axial force p in Eqs. (2) and (3) with Eq. (4), we can obtain the two equations of motion governing the deformed shape y and end motion e of the arch. It is noted that

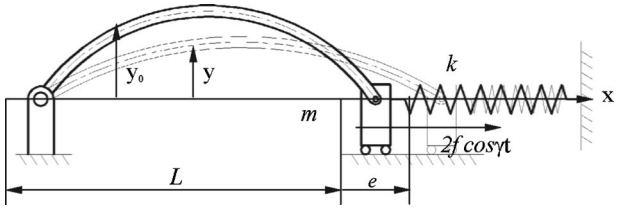

Fig. 2 Theoretical model of the arch-shaker assembly

Downloaded 16 Oct 2008 to 140.112.113.225. Redistribution subject to ASME license or copyright; see http://www.asme.org/terms/Terms_Use.cfm

Mettle formulated similar equations for a straight beam with end mass and under prescribed oscillating axial load in 1962 [16].

Equations (2)–(4) can be nondimensionalized by introducing the following dimensionless parameters (with asterisks)

$$(y^*, y_0^*, h^*) = \frac{1}{r}(y, y_0, h) \quad x^* = \frac{\pi x}{L} \quad t^* = \frac{\pi^2 t}{L^2}\sqrt{\frac{EI}{A\rho}}$$

$$(\gamma^*, \omega^*) = \frac{L^2}{\pi^2}\sqrt{\frac{A\rho}{EI}}(\gamma, \omega) \quad (p^*, f^*) = \frac{L^2}{\pi^2 EI}(p, f) \quad e^* = \frac{Le}{\pi^2 r^2}$$

$$m^* = \frac{I\pi^4 m}{L^3 A^2 \rho} \quad k^* = \frac{Lk}{EA} \quad \mu^* = \frac{\mu L^2}{\pi^2 \rho A r}\sqrt{\frac{\rho}{E}} \tag{5}$$

The parameters μ and ω are the damping and natural frequency of the arch-shaker system, which will be discussed later. r is the radius of gyration of the cross section of the arch. After substituting the above relations into Eqs. (2)–(4), and dropping all the superposed asterisks thereafter for simplicity, we obtain the two dimensionless equations of motion

$$y_{,tt} = -(y - y_0)_{,xxxx} + \left(e + \frac{1}{2\pi}\int_0^\pi [(y_{,x})^2 - (y_{0,x})^2]\right) y_{,xx} \tag{6}$$

$$m\ddot{e} = -\frac{1}{2\pi}\int_0^\pi [(y_{,x})^2 - (y_{0,x})^2]dx - (1+k)e + 2f\cos\gamma t \tag{7}$$

The boundary conditions for y at $x=0$ and π are

$$y(0) - y_0(0) = y_{,xx}(0) - y_{0,xx}(0) = y(\pi) - y_0(\pi) = y_{,xx}(\pi) - y_{0,xx}(\pi) = 0 \tag{8}$$

The dimensionless version of Eq. (1), the initial shape, can be written as

$$y_0 = \sum_{n=1}^{\infty} h_n \sin nx \tag{9}$$

It is assumed that the shape of the loaded arch can be expanded as

$$y(t) = y_0 + \sum_{n=1}^{\infty} \alpha_n(t)\sin nx \tag{10}$$

After substituting Eqs. (9) and (10) into Eqs. (6) and (7), multiplying Eq. (6) by $\sin nx$ and integrating from $x=0$ to π (Galerkin's procedure), we obtain the equations governing α_n and e

$$\ddot{\alpha}_n = -n^4\alpha_n - n^2(h_n + \alpha_n)\left[e + \frac{1}{4}\sum_{j=1}^{\infty} j^2(\alpha_j^2 + 2h_j\alpha_j)\right]$$

$$n = 1,2,3,\ldots \tag{11}$$

$$m\ddot{e} = -e(1+k) + 2f\cos\gamma t - \frac{1}{4}\sum_{j=1}^{\infty} j^2(\alpha_j^2 + 2h_j\alpha_j) \tag{12}$$

4 Natural Frequencies of the Assembly

The linearized version of Eqs. (11) and (12), without excitation, are

$$\ddot{\alpha}_n = -n^4\alpha_n - n^2\left(h_n e + \frac{1}{2}\sum_{j=1}^{\infty} j^2 h_n h_j \alpha_j\right) \quad n = 1,2,3,\ldots \tag{13}$$

Table 2 The first eight natural frequencies of the assembly. The second row (dimensionless) and the third row (dimensional) are calculated from Eqs. (13) and (14). The fourth row is measured from experiment.

i	1	2	3	4	5	6	7	8
ω_i^*	1.744	3.999	8.578	15.95	24.96	35.99	48.99	64.02
ω_i (Hz)	16.56	37.99	81.49	151.56	237.13	341.94	465.46	608.20
ω_i (Hz)	17	38	78	138	214	319	461	616

$$m\ddot{e} = -e(1+k) - \frac{1}{2}\sum_{j=1}^{\infty} j^2 h_j \alpha_j \tag{14}$$

From these two equations we can calculate the first eight natural frequencies $\omega_1 - \omega_8$ of the assembly, both dimensionless (ω_i^*, second row) and dimensional (ω_i, third row), as listed in Table 2. It is noted that the dimensionless natural frequency ω_i^* for $i \geqslant 2$ is very close to i^2, the ith natural frequency of the perfectly sinusoidal arch. The small deviation of the calculated natural frequencies from i^2 is caused by the geometrical imperfections.

One way to check whether the theoretical model for connection between the shaker and the arch is correct is to compare the above calculated natural frequencies of the arch-shaker assembly with those observed experimentally. Figure 3 shows the measured power spectrum of the arch itself without shaker (upper graph) and the arch-shaker assembly (lower graph). It is noted that the effect of the shaker attachment is to raise the first natural frequency from 10 to 17 Hz. The measured natural frequencies of the arch-shaker assembly are also recorded on the fourth row of Table 2. From the comparison of the third row and the fourth row of Table 2, we are confident that the mechanical model described in Fig. 2 and the estimated physical parameters for the shaker are not far from the truth.

5 Estimate of Damping

To simulate the motion of the assembly numerically, we still have to estimate the damping of the arch-shaker assembly. The dissipating mechanism of the system comes from the friction in the moving parts and the material damping in the arch. In order to accommodate the damping effect in the numerical simulation, we modify Eq. (11) by adding a damping parameter 2μ

$$\ddot{\alpha}_n = -2\mu\dot{\alpha}_n - n^4\alpha_n - n^2(h_n + \alpha_n)\left(e + \frac{1}{4}\sum_{j=1}^{\infty} j^2(\alpha_j^2 + 2h_j\alpha_j)\right)$$

$$n = 1,2,3,\ldots$$

In order to estimate the damping parameter of the arch-shaker assembly, we displace by hand the movable end of the arch a distance $e=-108$ (-0.29 mm) with the shaker attached, and then release it. The measured displacement history $y - y_0$ at the middle point of the arch is recorded as solid line in Fig. 4. For convenient reference, we present the measured results with both dimensionless parameters (left and bottom sides) and the physical ones (right and top sides). The same labeling style is adopted in all the figures involving experimental measurement. Since the oscillation frequency (17 Hz) corresponds to the first natural frequency of the arch-shaker assembly, we may assume that the first mode is dominant in the dynamic response in Fig. 4. The damping factor may be estimated from the decaying rate of the two peaks as signified by black dots. The heights of the two peaks are measured at $y_1 = 2.77$ (0.96 mm) and $y_2 = 1.90$ (0.66 mm). The ratio of the damping of the system μ to a critical damping μ_c is [17]

Downloaded 16 Oct 2008 to 140.112.113.225. Redistribution subject to ASME license or copyright; see http://www.asme.org/terms/Terms_Use.cfm

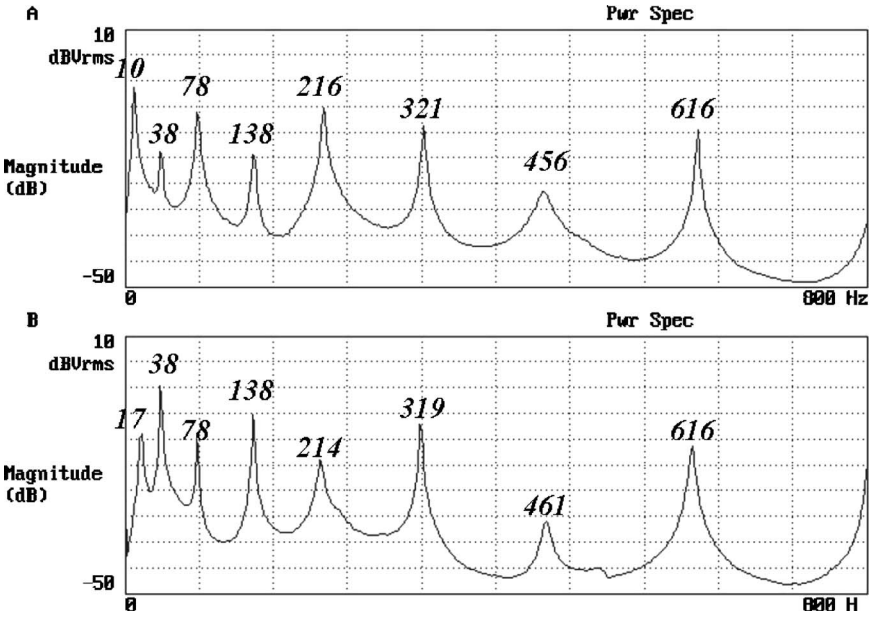

Fig. 3 Power spectrums of the arch itself (upper graph) and the arch-shaker assembly (lower graph)

$$\frac{\mu}{\mu_c} = \frac{\ln(y_1/y_2)}{\{(2\pi)^2 + [\ln(y_1/y_2)]^2\}^{1/2}} \tag{16}$$

The damping ratio in Eq. (16) is calculated as 0.06. The critical damping μ_c is estimated numerically by adjusting the damping parameter μ in Eq. (15) (using only one-mode approximation) until the response α_1 ceases to oscillate following an impulsive excitation. In this way the dimensionless critical damping μ_c is estimated as 3.0. As a consequence the damping of the assembly is calculated as $\mu=0.18$. The numerical result obtained by integrating Eqs. (12) and (15) based on this estimated damping is plotted in Fig. 4 as dashed line. Although this estimate may appear somewhat engineering-oriented, it is believed that the damping factor in our experimental setup is about this order.

6 Coupling Resonance

In the case when the arch is subjected to a lateral force with the excitation frequency close to a natural frequency of the arch, primary resonance will occur. Although in this section we also adjust the excitation frequency close to one of the natural frequencies ω_n $(n \geq 2)$ of the arch-shaker assembly, the arch is excited in the axial direction. In this situation, the nth mode of the assembly will not be excited directly by the excitation force. Instead, the nth mode will be excited indirectly by the axial mode after the axial mode is excited directly by the excitation force. It will be shown that the geometrical imperfection serves as the coupling factor between the lateral vibration and the axial excitation. Therefore, we choose to use the term "coupling resonance" here instead of "primary resonance." More physical insight regarding this matter can be found in the next section. In Fig. 5 we record the measured steady state amplitudes of the arch at 17 evenly spaced locations with closed dots "•" when the excitation frequency γ is close to the four natural frequencies $(\omega_2-\omega_5)$ of the arch, i.e., (*a*) 38 Hz, (*b*) 78 Hz, (*c*) 138 Hz, and (*d*) 216 Hz. The amplitude of excitation forces $2f$ in these four experiments are (*a*) 2.00 N, (*b*) 4.04 N, (*c*) 8.56 N, and (*d*) 10.68 N. The solid lines represent the numerical predictions from the complete theoretical model $(\alpha_1-\alpha_8)$ including the small imperfections. The dashed lines are the simplified model neglecting all the imperfections h_n with $n>1$.

Several comments can be made regarding Fig. 5. (1) By comparing the closed dots and the solid lines, we observe that the measured amplitudes agree fairly well with the complete-model prediction in all four cases. The worst agreement is observed in Fig. 5(*d*). (2) The amplitude profile is symmetric with respect to the midpoint when γ is close to the natural frequency of a symmetric mode, such as ω_3 and ω_5. On the other hand, the amplitude profile is asymmetric when γ is close to the natural frequency of an asymmetric mode, such as ω_2 and ω_4. (3) In all four cases the steady state vibrations contain two dominant components, i.e., α_1 and α_n. (4) If the small imperfections h_n with $n>1$ are neglected in the numerical simulation, all the corresponding components α_n will be suppressed to zero. This simplified model gives erroneous prediction as can be seen from the comparison of solid and dashed lines. The above observations indicate that in the case when the excitation frequency is close to the nth natural frequency, the corresponding small geometrical imperfection h_n should not be ignored.

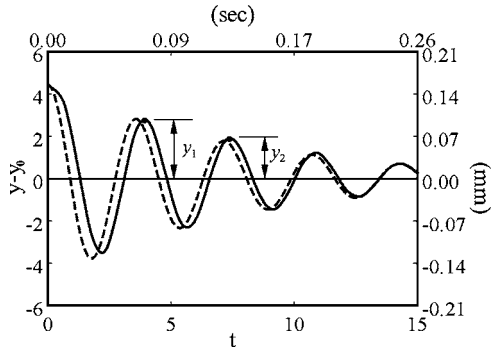

Fig. 4 Solid line is the measured lateral displacement history at the middle point of the arch after an initial displacement at the end of the arch-shaker assembly. Dashed line is the calculated response based on the estimated damping.

7 Multiple Scale Analysis for Coupling Resonance

To predict analytically the amplitude of vibration when the excitation frequency is close to ω_n, we retain only the coordinates α_1

Downloaded 16 Oct 2008 to 140.112.113.225. Redistribution subject to ASME license or copyright; see http://www.asme.org/terms/Terms_Use.cfm

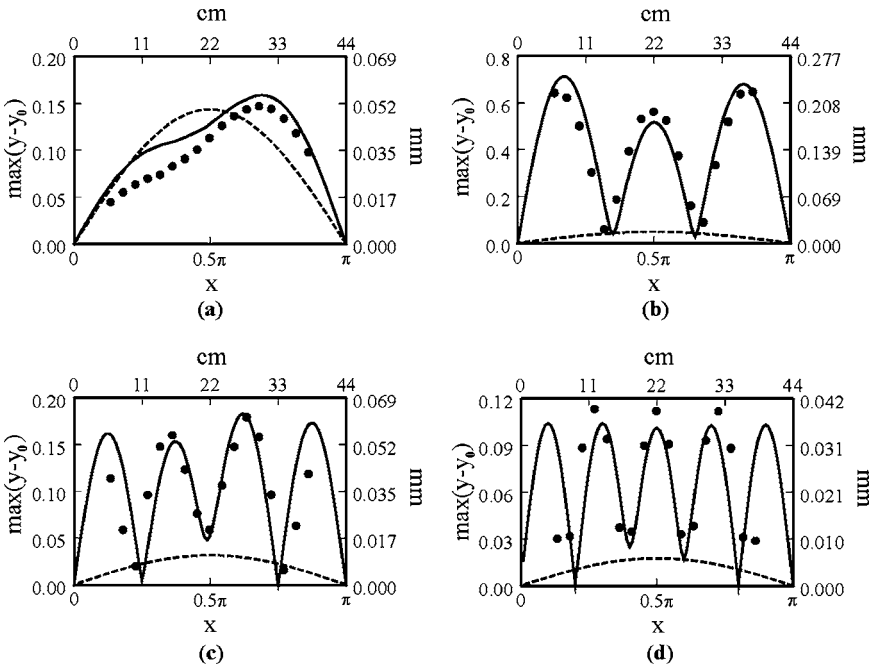

Fig. 5 Steady state amplitude profiles when the assembly is excited at (*a*) ω_1 =38 Hz, (*b*) ω_2=78 Hz, (*c*) ω_3=138 Hz, and (*d*) ω_4=216 Hz. Closed dots represent experimental measurements. Solid and dashed lines are the theoretical predictions including and excluding geometrical imperfections, respectively.

and α_n and neglect all other components in Eqs. (12) and (15). The three nontrivial equations of motion can be rewritten in the following form

$$\ddot{\alpha}_1 + \left(1 + \frac{h_1^2}{2}\right)\alpha_1 = -2\mu\dot{\alpha}_1 - \frac{1}{2}n^2 h_1 h_n \alpha_n - h_1 e - \frac{3}{4}h_1\alpha_1^2 - \frac{1}{4}n^2 h_1 \alpha_n^2 - \frac{1}{2}n^2 h_n \alpha_1 \alpha_n - \alpha_1 e - \frac{1}{4}\alpha_1^3 - \frac{1}{4}n^2 \alpha_1 \alpha_n^2 \tag{17}$$

$$\ddot{\alpha}_n + n^4\left(1 + \frac{h_n^2}{2}\right)\alpha_n = -2\mu\dot{\alpha}_n - \frac{1}{2}n^2 h_1 h_n \alpha_1 - n^2 h_n e - \frac{1}{4}n^2 h_n \alpha_1^2 - \frac{3}{4}n^4 h_n \alpha_n^2 - \frac{1}{2}n^2 h_1 \alpha_1 \alpha_n - n^2 \alpha_n e - \frac{1}{4}n^2 \alpha_1^2 \alpha_n - \frac{1}{4}n^4 \alpha_n^3 \tag{18}$$

$$m\ddot{e} + (1+k)e = -\tfrac{1}{2}h_1\alpha_1 - \tfrac{1}{2}n^2 h_n \alpha_n - \tfrac{1}{4}\alpha_1^2 - \tfrac{1}{4}n^2\alpha_n^2 + 2f\cos\gamma t \tag{19}$$

The numerical simulation based on Eqs. (17)–(19) is confirmed to agree well with the complete equations (12) and (15) when excitation frequency γ is close to ω_n. In the following we will use multiple scale method to study analytically the steady state amplitude and phase of α_n based on the simplified three-mode equations.

We first rescale Eqs. (17)–(19) by defining

$$(h_{n(n\geq 2)}, \mu, f, \alpha_1, \alpha_{n(n\geq 2)}, e) = \varepsilon(\hat{h}_{n(n\geq 2)}, \hat{\mu}, \hat{f}, \hat{\alpha}_1, \hat{\alpha}_{n(n\geq 2)}, \hat{e}) \tag{20}$$

ε is an artificial scale used to define the order of magnitude of various parameters. Equation (20) assumes that the three variables α_1, α_n, and e are of the same order of magnitude. After substituting relation (20) into Eqs. (17)–(19), the equations can be rewritten in the following form

$$\ddot{\hat{\alpha}}_1 + \left(1 + \frac{h_1^2}{2}\right)\hat{\alpha}_1 + h_1\hat{e} = -\varepsilon\left(2\hat{\mu}\dot{\hat{\alpha}}_1 + \frac{1}{2}n^2 h_1 \hat{h}_n \hat{\alpha}_n + \frac{3}{4}h_1\hat{\alpha}_1^2 + \frac{1}{4}n^2 h_1 \hat{\alpha}_n^2 + \hat{\alpha}_1\hat{e}\right) - \varepsilon^2\left(\frac{1}{2}n^2\hat{h}_n\hat{\alpha}_1\hat{\alpha}_n + \frac{1}{4}\hat{\alpha}_1^3 + \frac{1}{4}n^2\hat{\alpha}_1\hat{\alpha}_n^2\right) \tag{21}$$

$$\ddot{\hat{\alpha}}_n + n^4\hat{\alpha}_n = -\varepsilon\left(2\hat{\mu}\dot{\hat{\alpha}}_n + \tfrac{1}{2}n^2 h_1\hat{h}_n\hat{\alpha}_1 + n^2\hat{h}_n\hat{e} + \tfrac{1}{2}n^2 h_1\hat{\alpha}_1\hat{\alpha}_n + n^2\hat{\alpha}_n\hat{e}\right) - \varepsilon^2\left(\tfrac{1}{2}n^4\hat{h}_n^2\hat{\alpha}_n + \tfrac{1}{4}n^2\hat{h}_n\hat{\alpha}_1^2 + \tfrac{3}{4}n^4\hat{h}_n\hat{\alpha}_n^2 + \tfrac{1}{4}n^2\hat{\alpha}_1^2\hat{\alpha}_n + \tfrac{1}{4}n^4\hat{\alpha}_n^3\right) \tag{22}$$

$$m\ddot{\hat{e}} + (1+k)\hat{e} + \tfrac{1}{2}h_1\hat{\alpha}_1 = -\varepsilon\left(\tfrac{1}{2}n^2\hat{h}_n\hat{\alpha}_n + \tfrac{1}{4}\hat{\alpha}_1^2 + \tfrac{1}{4}n^2\hat{\alpha}_n^2\right) + 2\hat{f}\cos\gamma t \tag{23}$$

We now assume the following expansions for $\hat{\alpha}_1$, $\hat{\alpha}_n$, and $\hat{e}$,

$$\hat{\alpha}_1 = \alpha_{10}(T_0, T_1) + \varepsilon\alpha_{11}(T_0, T_1) \tag{24}$$

$$\hat{\alpha}_n = \alpha_{n0}(T_0, T_1) + \varepsilon\alpha_{n1}(T_0, T_1) \tag{25}$$

$$\hat{e} = e_0(T_0, T_1) + \varepsilon e_1(T_0, T_1) \tag{26}$$

where $T_n = \varepsilon^n t$. Substituting Eqs. (24)–(26) into Eqs. (21)–(23) and equating coefficients of like powers of ε yields ε^0

$$D_0^2\alpha_{10} + \left(1 + \frac{h_1^2}{2}\right)\alpha_{10} + h_1 e_0 = 0 \tag{27}$$

$$mD_0^2 e_0 + (1+k)e_0 + \tfrac{1}{2}h_1\alpha_{10} = \hat{f}e^{i\gamma T_0} + \hat{f}e^{-i\gamma T_0} \tag{28}$$

$$D_0^2\alpha_{n0} + n^4\alpha_{n0} = 0 \tag{29}$$

ε^1

Downloaded 16 Oct 2008 to 140.112.113.225. Redistribution subject to ASME license or copyright; see http://www.asme.org/terms/Terms_Use.cfm

$$D_0^2\alpha_{11}+\left(1+\frac{h_1^2}{2}\right)\alpha_{11}+h_1e_1 = -2D_0D_1\alpha_{10}-2\hat{\mu}D_0\alpha_{10} - \frac{1}{2}n^2h_1\hat{h}_n\alpha_{n0}-\frac{3}{4}h_1\alpha_{10}^2-\frac{1}{4}n^2h_1\alpha_{n0}^2-\alpha_{10}e_0 \quad (30)$$

$$mD_0^2e_1+(1+k)e_1+\tfrac{1}{2}h_1\alpha_{11} = -2mD_0D_1e_0-\tfrac{1}{2}n^2\hat{h}_n\alpha_{n0}-\tfrac{1}{4}\alpha_{10}^2 - \tfrac{1}{4}n^2\alpha_{n0}^2 \quad (31)$$

$$D_0^2\alpha_{n1}+n^4\alpha_{n1} = -2D_0D_1\alpha_{n0}-2\hat{\mu}D_0\alpha_{n0}-\tfrac{1}{2}n^2h_1\hat{h}_n\alpha_{10} - \tfrac{1}{2}n^2h_1\alpha_{10}\alpha_{n0}-n^2\hat{h}_ne_0-n^2\alpha_{n0}e_0 \quad (32)$$

where $D_n \equiv \partial/\partial T_n$. It is noted that Eqs. (27) and (28) are coupled equations of α_{10} and e_0, while Eq. (29) is an independent homogeneous equation of α_{n0}. The general solutions of Eqs. (27)–(29) can be written as

$$\alpha_{10}=A_1(T_1)e^{i\eta_1T_0}+B_1(T_1)e^{i\eta_2T_0}+\Lambda_1e^{i\gamma T_0}+\text{cc} \quad (33)$$

$$e_0=A_1(T_1)u_1e^{i\eta_1T_0}+B_1(T_1)u_2e^{i\eta_2T_0}+\Lambda_2e^{i\gamma T_0}+\text{cc} \quad (34)$$

$$\alpha_{n0}=A_n(T_1)e^{in^2T_0}+\text{cc} \quad (35)$$

where cc stands for the complex conjugates of the preceding terms. The parameters η_1 and η_2 are the two eigenvalues of Eqs. (27) and (28) (excluding the forcing term), with $(1,u_1)$ and $(1,u_2)$ being the corresponding eigenvectors. These parameters are calculated as

$$\eta_1=\pm\left(\frac{\Psi_1-\sqrt{\Psi_2+\Psi_1^2}}{4m}\right)^{1/2},\quad \eta_2=\pm\left(\frac{\Psi_1+\sqrt{\Psi_2+\Psi_1^2}}{4m}\right)^{1/2} \quad (36)$$

$$u_1=\frac{\Psi_3-\sqrt{\Psi_2+\Psi_1^2}}{4h_1m},\quad u_2=\frac{\Psi_3+\sqrt{\Psi_2+\Psi_1^2}}{4h_1m} \quad (37)$$

The constants Ψ_1, Ψ_2, and Ψ_3 are defined as

$$\Psi_1=2+2k+2m+h_1^2m,\quad \Psi_2=-8m(2+2k+h_1^2k),$$

$$\Psi_3=2+2k-2m-h_1^2m$$

The amplitudes Λ_1 and Λ_2 of the particular solutions are

$$\Lambda_1=\frac{-h_1}{\Phi(\gamma)}\hat{f},\quad \Lambda_2=\frac{2+h_1^2-2\gamma^2}{2\Phi(\gamma)}\hat{f} \quad (38)$$

where

$$\Phi(\gamma)=\left(1+\frac{h_1^2}{2}-\gamma^2\right)(1+k-m\gamma^2)-\frac{h_1^2}{2} \quad (39)$$

After substituting Eqs. (33)–(35) into Eqs. (30) and (31), following a solvability analysis we can conclude that $A_1\to 0$ and $B_1\to 0$ as $T_1\to\infty$ [18]. Therefore, the terms containing A_1 and B_1 in Eqs. (33) and (34) can be dropped. We now substitute Eqs. (33)–(35) into Eq. (32) and conclude that the secular term of Eq. (32) can be eliminated if

$$2iD_1A_ne^{in^2T_0}+2i\hat{\mu}A_ne^{in^2T_0}+\tfrac{1}{2}h_1\hat{h}_n\Lambda_1e^{i\gamma T_0}+\hat{h}_n\Lambda_2e^{i\gamma T_0}=0 \quad (40)$$

We assume that the excitation frequency γ is close to $\omega_n=n^2$, and can be expressed as

$$\gamma=n^2+\Delta\gamma=n^2+\varepsilon\sigma \quad (41)$$

where $\Delta\gamma$ is a small deviation from $\omega_n=n^2$, and is assumed to be of the order ε. σ is a detuning parameter. After using the above relation, Eq. (40) can be rearranged into the form

$$2iD_1A_n+2i\hat{\mu}A_n+\left(\tfrac{1}{2}h_1\hat{h}_n\Lambda_1+\hat{h}_n\Lambda_2\right)e^{i\sigma T_1}=0 \quad (42)$$

To solve A_n from Eq. (42), we express the complex variable A_n as

$$A_n=\tfrac{1}{2}a_ne^{i\theta_n} \quad (43)$$

where a_n and θ_n are real variables. Substituting Eq. (43) into Eq. (42) and equating the real part and imaginary part of Eq. (42) to zero, we obtain

$$a_n'+\hat{\mu}a_n=-\left(\tfrac{1}{2}h_1\hat{h}_n\Lambda_1+\hat{h}_n\Lambda_2\right)\sin\beta_n \quad (44)$$

$$\theta_n'a_n=\left(\tfrac{1}{2}h_1\hat{h}_n\Lambda_1+\hat{h}_n\Lambda_2\right)\cos\beta_n \quad (45)$$

where $\beta_n=\sigma T_1-\theta_n$. The superposed prime denotes the differentiation with respect to T_1. By assuming the existence of the steady state solution, we can let $a_n'=0$ and $\beta_n'=0$. As a consequence, the amplitude and phase of the steady state solution A_n can be solved from the following two algebraic equations

$$\hat{\mu}a_n=\left(\tfrac{1}{2}h_1\hat{h}_n\Lambda_1+\hat{h}_n\Lambda_2\right)\sin\beta_n \quad (46)$$

$$\sigma a_n=\left(\tfrac{1}{2}h_1\hat{h}_n\Lambda_1+\hat{h}_n\Lambda_2\right)\cos\beta_n \quad (47)$$

From Eqs. (46) and (47) we obtain the amplitude a_n and phase β_n as

$$a_n=\frac{\hat{h}_n(1-\gamma^2)}{\Phi(\gamma)\sqrt{\hat{\mu}^2+\sigma^2}}\hat{f} \quad (48)$$

$$\beta_n=\tan^{-1}\left(\frac{-\hat{\mu}}{\sigma}\right) \quad (49)$$

The final expressions of the steady state response can then be expressed in the following forms

$$\alpha_1=\frac{-2h_1}{\Phi(\gamma)}f\cos\gamma t \quad (50)$$

$$\alpha_n=\frac{h_n(1-\gamma^2)}{\Phi(\gamma)\sqrt{\mu^2+(\Delta\gamma)^2}}f\cos(\gamma t-\beta_n) \quad (51)$$

$$e=\frac{2+h_1^2-2\gamma^2}{\Phi(\gamma)}f\cos\gamma t \quad (52)$$

Therefore, to the order of our analysis, the amplitude of the mode α_n is proportional to the imperfection h_n. For a perfect sinusoidal arch with $h_n=0$, the mode α_n will never be excited even though the excitation frequency γ is equal to the natural frequency $\omega_n=n^2$.

The closed-form solutions for the amplitude and phase of α_n predicted by multiple scale analysis can be verified by numerically integrating the complete equations of motion Eqs. (12) and (15). The solid lines in Fig. 6 show the variation of (*a*) amplitude and (*b*) phase of α_4 as functions of frequency deviation parameter $\Delta\gamma$ predicted from the multiple scale analysis. The closed dots represent the amplitude and phase predicted from numerically integrating Eqs. (12) and (15). All the parameters (h_1, h_4, and f) used in the calculation correspond to the experiment described in Fig. 5(*c*). The analytical predictions via multiple scale analysis agree with the numerical integration quite well.

The above analysis also reveals the nature of the coupling resonance. In the last section we suggest that the resulted vibration should not be called "primary resonance" even though the excitation frequency of the axial force is close to the *n*th natural frequency of the arch. Our analysis in this section shows that the axial force excites the modes α_1 and e in a "nonresonant" manner (see Eqs. (33) and (34)). These two modes then excite the α_n-mode internally. However, it does not seem right to call it internal resonance because internal resonance is usually referred

Downloaded 16 Oct 2008 to 140.112.113.225. Redistribution subject to ASME license or copyright; see http://www.asme.org/terms/Terms_Use.cfm

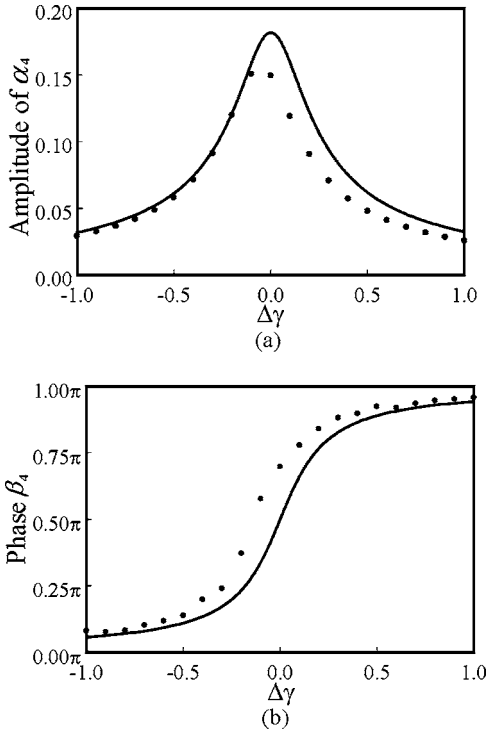

Fig. 6 (*a*) Amplitude and (*b*) phase of α_4 as functions of the frequency deviation $\Delta\gamma$. The solid lines are from multiple scale analysis. The closed dots are from numerically integrating the complete equations of motion.

to the situation when the natural frequencies involved possess certain relations [11–13]. The key for the resonance discussed in this section to occur is the geometrical imperfection h_n, which couples the lateral vibration with the axial excitation. Therefore, we choose the term "coupling resonance." The indirectly excited mode α_n is found to be of the same order of magnitude of the directly excited modes α_1 and e.

8 Parametric Resonance

In this section we direct our attention to the case when the excitation frequency is close to $2\omega_2$ (76 Hz). The amplitude of the excitation force $2f$ in this experiment is fixed at 40.06 N. We record the steady state time history at two locations symmetric with respect to and 11 cm (a quarter of the total length) away from the midpoint simultaneously and subtract one from the other. By this procedure all the signals from the symmetric modes (α_1 and α_3 particularly) will be canceled out. Therefore, the resulted signal contains mainly the α_2-mode, whose amplitude is recorded in Fig. 7. We first sweep the excitation frequency from a little higher than 76 Hz to a little lower than 76 Hz. The amplitude of the resulted signal is denoted by the symbol "×." It is observed that in this "sweeping-down" process, the amplitude of α_2 changes from very small to a noticeable amount when the excitation frequency is at 78 Hz, slightly above $2\omega_2$. It is noted that 78 Hz happens to be the natural frequency ω_3 of the arch. Therefore, the overall vibration amplitude is large, as have been demonstrated in Fig. 5(*b*). However, the net signal after subtraction is still relatively small. The amplitude of α_2 continues to increase when the excitation frequency decreases. In another experiment we sweep the excitation frequency from 73 Hz upward. The measured amplitude is recorded by the symbol "•." In the lower end of this "sweeping-up" process the measured amplitude is very small (about 0.1 mm) until the excitation frequency reaches 74.2 Hz, at which the measured amplitude experiences an obvious jump to 2.77 mm. After the jump, the measured amplitude decreases

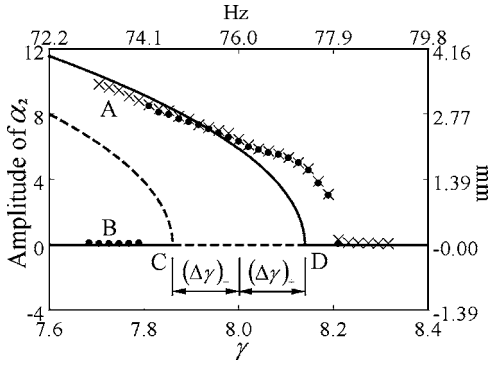

Fig. 7 Steady state amplitude of component α_2. "•" represents the measurement during the sweeping-down process. "×" represents the measurement during the sweeping-up process. Solid (stable) and dashed (unstable) lines are multiple scale predictions.

gradually as the excitation frequency continues to sweep up, following more or less the locus recorded during the previous "sweeping-down" experiment. Obviously at frequency below 74.2 Hz, there exist two steady state solutions simultaneously.

To investigate these two steady state responses further, we measured the overall amplitude profiles at frequency 73.4 Hz, the points *A* and *B* in Fig. 7. We can easily switch the arch vibration between states *A* and *B* by disturbing the arch with hands. Figure 8 shows the amplitude profiles of these two steady states. Symbols "×" are for state *A*, while symbols "•" are for state *B*. In Fig. 9 we record the time history of these two responses at location $x = 11$ cm. We found that in state *A* the dominant frequency is 36.7 Hz, while in response *B* the dominant frequency appears to

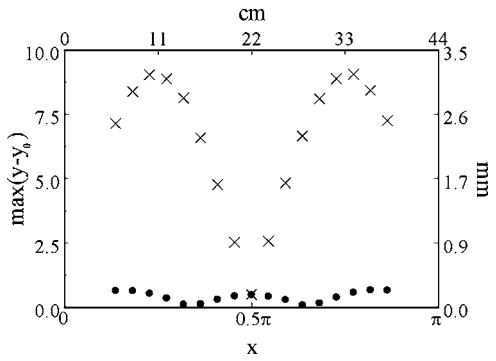

Fig. 8 Amplitude profiles corresponding to the two steady states *A* and *B* in Fig. 7

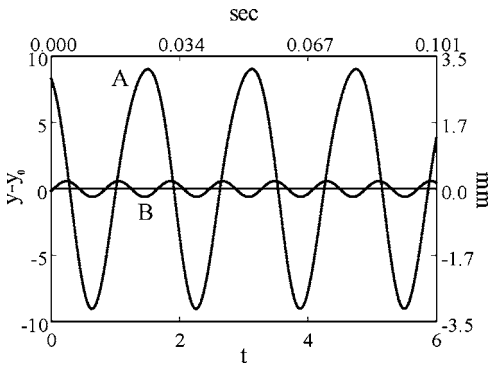

Fig. 9 Time history of the two states *A* and *B* in Fig. 7 measured at location 11 cm from the midpoint

Downloaded 16 Oct 2008 to 140.112.113.225. Redistribution subject to ASME license or copyright; see http://www.asme.org/terms/Terms_Use.cfm

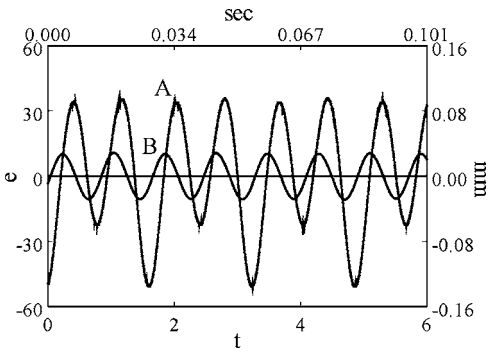

Fig. 10 Time history of the end motion of the two states *A* and *B* in Fig. 7

be two times of the state A. By inspecting Figs. 8 and 9 we can determine that the dominant component in the amplitude profile corresponding to state A is apparently $\sin 2x$. We can also identify the minor components in the response A as $\sin x$ and $\sin 3x$. To determine that the response contains the components $\sin x$ and $\sin 3x$, we record the time history at two points symmetrical with respect to the midpoint simultaneously and add them up (instead of subtracting one from another as described in Fig. 7). This adding process will eliminate the dominant component $\sin 2x$. By repeating this process for eight pairs of locations we obtain an amplitude profile that contains mostly the $\sin x$ and $\sin 3x$ modes. For the amplitude profile corresponding to state B the dominant component is $\sin 3x$. The reason why the mode $\sin 3x$ is present in both responses A and B is because the excitation frequency $2\omega_2$ happens to be close to ω_3.

It is noted that the vibration amplitude of steady state A is almost ten times larger than that of state B, as seen from Fig. 9. We also record the time history of the end motion for these two states in Fig. 10. It is noted that for state A with large lateral vibration the end motion is no longer harmonic. On the other hand, the end motion of state B is still quite close to harmonic.

9 Multiple Scale Analysis for Parametric Resonance

As discussed in Sec. 8, the reason why the mode $\sin 3x$ is present in the measured response is because the excitation frequency $2\omega_2$ happens to be close to ω_3. If we exclude this complicating factor, we may conclude that α_1 and α_2 will be two dominant components when the excitation frequency γ is close to $2\omega_2$. Further numerical calculation shows that in this case the geometrical imperfection has only minimal effect on the final steady state response. To analytically predict the steady state solutions and gain more physical insight into the jump phenomenon observed in the experiment, we employ again the multiple scale analysis on this case.

As in Sec. 7 we start with the three-mode equations (17)–(19), except that the imperfection h_n is set to be zero for simplicity. The numerical simulation based on the three-mode equations with $h_n = 0$ is found to agree quite well with the complete Eqs. (12) and (15) when excitation frequency γ is close to $2\omega_n$. In this case we rescale the parameters in a somewhat different manner

$$\alpha_n = \varepsilon \hat{\alpha}_n \tag{53}$$

$$(\mu, f, \alpha_1, e) = \varepsilon^2(\hat{\mu}, \hat{f}, \hat{\alpha}_1, \hat{e}) \tag{54}$$

In other words, we assume that α_n is one order of magnitude larger than those parameters listed in Eq. (54). This assumption is based mainly on the experimental observation. After substituting Eqs. (53) and (54) into Eqs. (17)–(19) the equations can be rewritten in the following form

$$\ddot{\hat{\alpha}}_1 + \left(1 + \frac{h_1^2}{2}\right)\hat{\alpha}_1 + h_1\hat{e} = -\frac{1}{4}n^2 h_1 \hat{\alpha}_n^2 - \varepsilon^2\left(2\hat{\mu}\dot{\hat{\alpha}}_1 + \hat{\alpha}_1\hat{e} + \frac{3}{4}h_1\hat{\alpha}_1^2\right) \tag{55}$$

$$\ddot{\hat{\alpha}}_n + n^4\hat{\alpha}_n = -\varepsilon^2\left(2\hat{\mu}\dot{\hat{\alpha}}_n + \tfrac{1}{2}n^2 h_1\hat{\alpha}_1\hat{\alpha}_n + n^2\hat{\alpha}_n\hat{e} + \tfrac{1}{4}n^4\hat{\alpha}_n^3\right) \tag{56}$$

$$m\ddot{\hat{e}} + (1+k)\hat{e} + \tfrac{1}{2}h_1\hat{\alpha}_1 = 2\hat{f}\cos\gamma t - \tfrac{1}{4}n^2\hat{\alpha}_n^2 - \varepsilon^2\left(\tfrac{1}{4}\hat{\alpha}_1^2\right) \tag{57}$$

We now assume the following expansions for $\hat{\alpha}_1$, $\hat{\alpha}_n$, and $\hat{e}$

$$\hat{\alpha}_1 = \alpha_{10}(T_0, T_2) + \varepsilon^2\alpha_{12}(T_0, T_2) \tag{58}$$

$$\hat{\alpha}_n = \alpha_{n0}(T_0, T_2) + \varepsilon^2\alpha_{n2}(T_0, T_2) \tag{59}$$

$$\hat{e} = e_0(T_0, T_2) + \varepsilon^2 e_2(T_0, T_2) \tag{60}$$

Following a similar procedure as described in Sec. 7, and equating coefficients of like powers of ε yields ε^1

$$D_0^2\alpha_{n0} + n^4\alpha_{n0} = 0 \tag{61}$$

ε^2

$$D_0^2\alpha_{10} + \left(1 + \frac{h_1^2}{2}\right)\alpha_{10} + h_1 e_0 = -\frac{n^2}{4}h_1\alpha_{n0}^2 \tag{62}$$

$$mD_0^2 e_0 + (1+k)e_0 + \frac{1}{2}h_1\alpha_{10} = \hat{f}e^{i\gamma T_0} + \hat{f}e^{-i\gamma T_0} - \frac{n^2}{4}\alpha_{n0}^2 \tag{63}$$

ε^3

$$D_0^2\alpha_{n2} + n^4\alpha_{n2} = -2D_0D_2\alpha_{n0} - 2\hat{\mu}D_0\alpha_{n0} - n^2\alpha_{n0}e_0 - \frac{n^2}{2}h_1\alpha_{10}\alpha_{n0} - \frac{n^4}{4}\alpha_{n0}^3 \tag{64}$$

The general solution of the homogeneous equation (61) can be written as

$$\alpha_{n0} = A_n(T_2)e^{in^2T_0} + \text{cc} \tag{65}$$

After substituting Eq. (65) into Eqs. (62) and (63) we can solve for α_{10} and e_0 as

$$\alpha_{10} = A_1 e^{i\eta_1 T_0} + B_1 e^{i\eta_2 T_0} + \Lambda_{11}e^{i\gamma T_0} + \Lambda_{12}e^{2in^2T_0} + \Lambda_{13} + \text{cc} \tag{66}$$

$$e_0 = u_1A_1e^{i\eta_1T_0} + u_2B_1e^{i\eta_2T_0} + \Lambda_{21}e^{i\gamma T_0} + \Lambda_{22}e^{2in^2T_0} + \Lambda_{23} + \text{cc} \tag{67}$$

The parameters η_1, η_2, u_1, and u_2 have been defined in Eqs. (36) and (37). Λ_{ij} are defined as

$$\Lambda_{11} = -\frac{h_1\hat{f}}{\Phi(\gamma)}, \quad \Lambda_{21} = \frac{(2 + h_1^2 - 2\gamma^2)\hat{f}}{2\Phi(\gamma)}$$

$$\Lambda_{12} = -\frac{n^2h_1(k - 4mn^4)}{4\Phi(2n^2)}A_n^2, \quad \Lambda_{22} = -\frac{n^2(1-4n^4)}{4\Phi(2n^2)}A_n^2$$

$$\Lambda_{13} = -\frac{n^2h_1k}{4\Phi(0)}A_n\bar{A}_n, \quad \Lambda_{23} = -\frac{n^2}{4\Phi(0)}A_n\bar{A}_n$$

where the function $\Phi(\cdot)$ has been defined in Eq. (39). We assume that the excitation frequency is close to $2\omega_n$, i.e.

$$\gamma = 2n^2 + \Delta\gamma = 2n^2 + \varepsilon^2\sigma \tag{68}$$

Substituting Eqs. (65)–(68) into Eq. (64), the solvability condition for α_{n2} can be obtained as

$$A_n' + C_1A_n + iC_2\bar{A}_ne^{i\sigma T_2} + iC_3A_n^2\bar{A}_n = 0 \tag{69}$$

where the coefficients C_i are

Downloaded 16 Oct 2008 to 140.112.113.225. Redistribution subject to ASME license or copyright; see http://www.asme.org/terms/Terms_Use.cfm

$$C_1 = \hat{\mu}, \quad C_2 = \frac{(\gamma^2 - 1)}{2\Phi(\gamma)}\hat{f},$$

$$C_3 = \frac{n^2}{16}\left(\frac{h_1^2(k - 4mn^4) + 2(1 - 4n^4)}{\Phi(2n^2)} + \frac{2kh_1^2 + 4}{\Phi(0)} - 6\right)$$

The superposed prime in Eq. (69) represents derivative with respect to T_2. To solve the homogeneous equation (69) we express A_n in the same form as in Eq. (43). After substituting Eq. (43) into Eq. (69) we obtain the two equations for the amplitude a_n and θ_n

$$a_n' + C_1 a_n - C_2 a_n \sin\beta_n = 0 \tag{70}$$

$$a_n(4\theta_n' + 4C_2 \cos\beta_n + C_3 a_n^2) = 0 \tag{71}$$

where $\beta_n = \sigma T_2 - 2\theta_n$. The amplitude and phase of the steady state solutions can then be solved from

$$a_n(C_1 - C_2 \sin\beta_n) = 0 \tag{72}$$

$$a_n(2\sigma + 4C_2 \cos\beta_n + C_3 a_n^2) = 0 \tag{73}$$

Two types of solutions can be found from Eqs. (72) and (73). The first is the trivial solution $a_n = 0$. In this case the mode α_n will not be excited. The second solution is nontrivial, where

$$\beta_n = \sin^{-1}\left(\frac{C_1}{C_2}\right) \tag{74}$$

$$a_n = \left(\frac{-2\sigma \pm 4\sqrt{C_2^2 - C_1^2}}{C_3}\right)^{1/2} \tag{75}$$

To determine the stability of the above trivial and nontrivial steady state solutions, we express A_n in Eq. (69) as the superposition of the steady state solution A_{ns} and a small disturbance $\tilde{A}_n$

$$A_n = A_{ns} + \tilde{A}_n \tag{76}$$

After substituting Eq. (76) into Eq. (69) and linearizing the equation with respect to $\tilde{A}_n$, we obtain the linear equation for $\tilde{A}_n$

$$\tilde{A}_n' + C_1\tilde{A}_n + iC_2\bar{\tilde{A}}_n e^{i\sigma T_2} + iC_3(2A_{ns}\bar{A}_{ns}\tilde{A}_n + A_{ns}^2\bar{\tilde{A}}_n) = 0 \tag{77}$$

A_{ns} in Eq. (77) is the trivial and nontrivial solutions solved previously. After expressing $\tilde{A}_n$ in the form $\tilde{A}_n = (a_{nR} + ia_{nI})e^{(1/2)i\sigma T_2}$, Eq. (77) can be rewritten as two real equations

$$a_{nR}' + \left(C_1 + \tfrac{1}{4}C_3 a_n^2 \sin\beta_n\right)a_{nR} + \left(C_2 - \tfrac{1}{2}\sigma - \tfrac{1}{4}C_3 a_n^2(2 - \cos\beta_n)\right)a_{nI} = 0 \tag{78}$$

$$\left(C_2 + \frac{1}{2}\sigma + \frac{1}{4}C_3 a_n^2(2 + \cos\beta_n)\right)a_{nR} + a_{nI}' + \left(C_1 - \frac{1}{4}C_3 a_n^2 \sin\beta_n\right)a_{nI} = 0 \tag{79}$$

a_n and phase β_n in Eqs. (78) and (79) are the amplitude and phase expressed in Eqs. (74) and (75). By solving the eigenvalues of Eqs. (78) and (79) we can determine the stability of the steady state solutions. The final expressions of the steady state response of α_n are expressed in the following form

$$\alpha_n = \left(\frac{-2\Delta\gamma \pm 4\sqrt{\left(\frac{(\gamma^2 - 1)}{2\Phi(\gamma)}f\right)^2 - \mu^2}}{C_3}\right)^{1/2} \cos\left(\frac{\gamma - \beta_n}{2}t\right) \tag{80}$$

After substituting the physical parameters corresponding to the experiment shown in Fig. 7, we can plot the calculated amplitude of the steady state solution α_2 as solid (stable) and dashed (unstable) lines. Two bifurcation points can be observed in Fig. 7. Point C is a subcritical pitch-fork bifurcation point, while D is a supercritical pitch-fork bifurcation point. The two bifurcation frequencies are $2n^2 + (\Delta\gamma)_+$ and $2n^2 + (\Delta\gamma)_-$, (recall that $n = 2$ in this case) where frequency deviations $(\Delta\gamma)_+$ and $(\Delta\gamma)_-$ can be calculated as

$$(\Delta\gamma)_\pm = \pm 2\sqrt{\left[\frac{(\gamma^2 - 1)}{2\Phi(\gamma)}f\right]^2 - \mu^2} \tag{81}$$

In evaluating $(\Delta\gamma)_\pm$ from Eq. (81) we can replace γ by $2n^2$ for simplicity. The resulting error in doing so is less than 0.5%. It is noted that fairly good agreement in amplitudes between the experimental results and analytical prediction can be observed. Although the bifurcation points are off somewhat, the multiple scale analysis predicts the jump phenomenon quite well.

10 Conclusions

In this paper we study the nonlinear vibration of a shallow arch with one end attached to an electro-mechanical shaker. The arch is excited in the axial direction. In the experiment we can control the excitation force on the end mass but not the end motion of the arch. Attention is focused on two cases, i.e., the coupling resonance and parametric resonance. In the case of coupling resonance the excitation frequency is close to the natural frequency of the nth mode. In the parametric resonance case, the excitation frequency is two times the nth natural frequency. Experimental, numerical, and analytical methods are used to look into the physical insight of these complicated nonlinear oscillation phenomena. Several conclusions can be summarized in the following.

(1) Geometrical imperfection is the key for the coupling resonance to occur. For a perfect sinusoidal arch, the nth mode will not be excited even when the excitation frequency is close to its corresponding natural frequency. When geometrical imperfection exists, which is almost inevitable in the real world, the first mode and the axial mode will be excited directly by the excitation in a "nonresonant" manner, and then these modes in turn excite the nth mode internally.
(2) In the case of parametric resonance, two stable steady state solutions can exist simultaneously when the excitation frequency is slightly lower than two times the nth natural frequency. As a consequence jump phenomenon is observed when the excitation frequency sweeps upward. The effect of geometrical imperfection on the steady state response is minimal in this case. While only the stable steady states can be realized in the experiment, the multiple scale method can predict both the stable and unstable solutions.

Acknowledgment

The results presented here were obtained in the course of research supported by a grant from the National Science Council of the Republic of China.

References

[1] Timoshenko, S. P., 1935, "Buckling of Flat Curved Bars and Slightly Curved Plates," ASME J. Appl. Mech., **2**, pp. 17–20.
[2] Hoff, N. J., and Bruce, V. G., 1954, "Dynamic Analysis of the Buckling of Laterally Loaded Flat Arches," J. Math. Phys., **32**, pp. 276–288.
[3] Simitses, G. J., 1986, *Elastic Stability of Structures*, Krieger, Malabar, FL, Chap. 7.
[4] Simitses, G. J., 1990, *Dynamic Stability of Suddenly Loaded Structures*, Springer, New York.
[5] Chen, J. S., and Liao, C. Y., 2005, "Experiment and Analysis on the Free Dynamics of a Shallow Arch After an Impact Load at the End," ASME J. Appl. Mech., **72**, pp. 54–61.
[6] Huang, N. C., 1972, "Dynamic Buckling of Some Elastic Shallow Structures Subject to Periodic Loading with High Frequency," Int. J. Solids Struct., **8**, pp. 315–326.
[7] Plaut, R. H., and Hsieh, J. C., 1985, "Oscillations and Instability of a Shallow Arch Under Two-Frequency Excitation," J. Sound Vib., **102**, pp. 189–201.
[8] Blair, K. B., Krousgrill, C. M., and Farris, T. N., 1996, "Non-Linear Dynamic Response of Shallow Arches to Harmonic Forcing," J. Sound Vib., **194**, pp.

Downloaded 16 Oct 2008 to 140.112.113.225. Redistribution subject to ASME license or copyright; see http://www.asme.org/terms/Terms_Use.cfm

353–367.
[9] Thomsen, J. J., 1992, "Chaotic Vibrations of Non-Shallow Arches," J. Sound Vib., **153**, pp. 239–258.
[10] Bolotin, V. V., 1964, *The Dynamic Stability of Elastic Systems*, Holden-Day, San Francisco.
[11] Tien, W. M., Sri Namachchivaya, N., and Bajaj, A. K., 1994, "Non-Linear Dynamics of a Shallow Arch under Periodic Excitation—I. 1:1 Internal Resonance," Int. J. Non-Linear Mech., **29**, pp. 367–386.
[12] Tien, W. M., Sri Namachchivaya, N., and Bajaj, A. K., 1994, "Non-Linear Dynamics of a Shallow Arch under Periodic Excitation—II. 1:2 Internal Resonance," Int. J. Non-Linear Mech., **28**, pp. 349–366.
[13] Bi, Q., and Dai, H. H., 2000, "Analysis of Nonlinear Dynamics and Bifurcations of a Shallow Arch Subjected to Periodic Excitation With Internal Resonance," J. Sound Vib., **233**, pp. 557–571.
[14] Malhotra, N., and Sri Namachchivaya, N., 1997, "Chaotic Dynamics of Shallow Arch Structures Under 1:1 Resonance," J. Eng. Mech., **123**, pp. 620–627.
[15] Malhotra, N., and Sri Namachchivaya, N., 1997, "Chaotic Dynamics of Shallow Arch Structures under 1:2 Resonance," J. Eng. Mech., **123**, pp. 612–619.
[16] Mettler, E., 1962, "Dynamic Buckling," in *Handbook of Engineering Mechanics*, W. Flugge, ed., McGraw Hill, New York, Chap. 62.
[17] Rao, S. S., 1995, *Mechanical Vibrations*, 3rd ed., Addision-Wesley, Reading, MA.
[18] Yang, C.-H., 2005, "Nonlinear Vibration of a Shallow Arch Under Periodic Excitation at One End," MS thesis, Department of Mechanical Engineering, National Taiwan University, Taipei, Taiwan.

Downloaded 16 Oct 2008 to 140.112.113.225. Redistribution subject to ASME license or copyright; see http://www.asme.org/terms/Terms_Use.cfm